A large pool of releasable vesicles in a cortical glutamatergic synapse

Stefan Hallermann, Christian Pawlu, Peter Jonas*, and Manfred Heckmann

Physiologisches Institut, Universität Freiburg, D-79104 Freiburg, Germany

Communicated by Roger A. Nicoll, University of California, San Francisco, CA, May 12, 2003 (received for review March 25, 2003)

To probe exocytosis at a cortical glutamatergic synapse, we made capacitance measurements in whole-cell recorded hippocampal mossy fiber terminals. Evaluation of different methods by using a morphology-based equivalent electrical model revealed that quantitative capacitance measurements are possible in this presynaptic structure. Voltage pulses leading to presynaptic Ca^{2+} inflow evoked large capacitance signals that showed saturation with increasing pulse duration. The mean peak capacitance increase was 100 fF, corresponding to a pool of ≈1,400 releasable vesicles. Thus hippocampal mossy fiber synapses have a vesicular ''maxipool.'' Large pool size and rapid vesicle recycling may underlie the uniquely large extent of activity-dependent plasticity in this synapse.

Our current knowledge about fundamental aspects of synaptic transmission is largely based on the highly detailed analysis of a limited number of synapse types, such as the neuromuscular junction, the squid giant synapse, the retinal bipolar cell synapse, and the calyx of Held (1–10). These synapses offer direct access to presynaptic terminals, which has greatly facilitated the mechanistic analysis of transmitter release (e.g., ref. 5). However, glutamatergic synapses in higher brain circuits differ substantially from these ''model synapses'' in both morphological and functional aspects; for example, in the properties and extent of synaptic plasticity (11–13). Thus, to obtain a complete picture of cortical synaptic transmission and plasticity, direct examination of cortical synapses is unavoidable.

Electrical recording of postsynaptic currents is the standard assay to probe transmitter release. However, this approach has limitations, especially when applied to cortical synapses. The postsynaptic assay is difficult to calibrate, because neither the number of transmitter molecules in a synaptic vesicle nor the density of postsynaptic receptors are precisely known. The assay may be nonlinear, because of saturation or desensitization of postsynaptic receptors (14, 15). Furthermore, different modes of transmitter release (e.g., kiss-and-run versus full fusion; refs. 16 and 17) cannot be distinguished, and endocytosis cannot be measured directly. In synapses with ''giant'' presynaptic terminals, presynaptic capacitance measurements have been used to probe exo- and endocytosis quantitatively (9, 14, 18, 19). However, application of this technique to cortical presynaptic terminals is not trivial. The sensitivity of the technique needs to be optimized, because the expected capacitance changes are near the absolute limits of resolution. Furthermore, the interpretation of recorded signals must take into account the multicompartment electrical structure of the presynaptic terminals (20, 21).

To quantitatively measure exo- and endocytosis at a cortical glutamatergic synapse in real time, we performed presynaptic capacitance measurements in hippocampal mossy fiber terminals (22–26). After validation of capacitance measurement methods by using equivalent electrical models, we addressed the following fundamental questions: How large is the releasable pool of vesicles at mossy fiber terminals (27–30)? Is the release rate derived from capacitance measurements more consistent with univesicular or multivesicular release (31, 32)? How fast is endocytosis after depletion of the releasable vesicle pool (33)?

Methods

Recording from Mossy Fiber Terminals in Acute Hippocampal Slices. Transverse 250- to 300-μm-thick slices were cut from the hippocampi of 20- to 26-day-old Wistar rats with a custom-built vibratome (34). The animals were killed by decapitation in accordance with national and institutional guidelines. For the dissection and storage of the slices a solution containing 64 mM NaCl, 25 mM $NaHCO_3$, 10 mM glucose, 120 mM sucrose, 2.5 mM KCl, 1.25 mM NaH_2PO_4, 0.5 mM $CaCl_2$, and 7 mM $MgCl_2$ (95% O_2/5% CO_2) was used. The slices were incubated for 30 min at 35°C and then held at room temperature for <3 h. During experiments, the slices were superfused with a physiological extracellular solution containing 125 mM NaCl, 25 mM $NaHCO_3$, 25 mM glucose, 2.5 mM KCl, 1.25 mM NaH_2PO_4, 2 mM $CaCl_2$, and 1 mM $MgCl_2$ (95% O_2/5% CO_2). Recordings were made from mossy fiber terminals in the *stratum lucidum* of the hippocampal cornu ammonis area 3 (CA3) region as described (22, 23). Patch pipettes were pulled from borosilicate glass tubing (2-mm outer diameter, 0.5-mm wall thickness) and filled with an intracellular solution containing 155 mM CsCl, 6.25 mM $MgCl_2$, 0.26 mM EGTA, 0.04 mM $CaCl_2$, 4 mM Na_2ATP, 0.3 mM NaGTP, and 10 mM Hepes; the pH was adjusted to 7.3 with CsOH. This composition theoretically gives ≈50 nM free Ca^{2+}, ≈0.2 mM free EGTA, and ≈2 mM free Mg^{2+} (35). The pipette open-tip resistance was 5–12 MΩ. All recordings were made in a bath solution containing 105 mM NaCl, 25 mM $NaHCO_3$, 25 mM glucose, 2.5 mM KCl, 1.25 mM NaH_2PO_4, 2 mM $CaCl_2$, 1 mM $MgCl_2$, 1 μM tetrodotoxin (TTX), 20 mM tetraethylammonium chloride (TEA), and 5 mM 4-aminopyridine (4AP); to avoid depolarization of the recorded terminals, this solution was applied directly after whole-cell voltage clamp was established. To minimize pipette capacitance, care was taken to maintain the bath solution at the lowest possible level. Recordings were made with an EPC-9/2 amplifier (HEKA Electronics, Lambrecht/Pfalz, Germany) in the voltage-clamp mode. The pipette capacitance was compensated in the cell-attached configuration (''C-fast''; time constants 1–3 μs). All measurements were made at 21 ± 2°C, unless otherwise specified (34°C in Fig. 3*F*). Data are reported as mean ± SEM, unless otherwise noted. Significance was assessed by using a two-sided Mann–Whitney test.

Development of Morphology-Based and Reduced Equivalent Models of Mossy Fiber Terminals. Current transients were evoked by square pulses with alternating amplitudes of ±20 mV from a holding potential of −100 mV. The internal two-pole Bessel filter for stimulus voltage was set to 2 μs, the three-pole Bessel filter for current was set to 100 kHz, and the sampling frequency was set to 200 kHz. Responses to positive and negative pulses

Abbreviations: ΔC_m, capacitance change; C_m, membrane capacitance; R_a, access resistance; R_m, membrane resistance.

See commentary on page 8618.

*To whom correspondence should be addressed at: Physiologisches Institut, Universität Freiburg, Hermann-Herder-Strasse 7, D-79104 Freiburg, Germany. E-mail: peter.jonas@physiologie.uni-freiburg.de.

were averaged separately and plotted against each other for corresponding time points; experiments with signs of nonlinearity (slope <0.99 or >1.01) were discarded (5 of 17 boutons). For subsequent analysis, average responses to positive pulses (for 0.02 ms $< t \leq$ 5 ms) were used. To obtain a morphology-based model, boutons were filled with 0.1% biocytin during recording (36). Slices were fixed with 2.5% paraformaldehyde, 1.25% glutaraldehyde, and 15% picric acid and were developed with avidin-biotinylated horseradish peroxidase complex (ABC, Vector Laboratories), using 0.05% 3,3′-diaminobenzidine as chromogen. One biocytin-filled bouton was selected for reconstruction with a light microscope (×100 oil immersion objective; NEUROLUCIDA 3 system, MicroBrightField, Colchester, VT). No correction was made for shrinkage. The diameter of the axon was 0.14–0.40 μm, consistent with electron-microscopic data (34). After conversion into NEURON format, access resistance, shunt conductance, and specific parameters C_m, R_i, and R_m were determined by direct fitting of the current transients (37) with Fitpraxis of NEURON 5.1 (ref. 38; 1-μs time step). Current transients were also fitted by simple equivalent electrical models. A one-compartment model, a two-compartment model, a model with one compartment and an attached cylinder, and a three-compartment model were tested. For the two- and three-compartment models, the circuit was assembled in the Laplace domain, and the current as a function of time was obtained by inverse Laplace transformation. For the compartment-cylinder model, the current transient was calculated as reported (39). Direct fitting was performed with MATHEMATICA 4.1 (Wolfram Research, Champaign, IL), minimizing the sum of squares of differences between measured and simulated traces. To achieve uniqueness, the number of free parameters was reduced by homogeneity assumptions ($R_m C_m$ = const., which gives five free parameters for both the two-compartment model and the compartment-cylinder model and seven free parameters for the three-compartment model).

Evaluation of Different Methods for Capacitance Measurements by Using the Morphology-Based Model. The performance of square-pulse and sine-wave methods was evaluated by using the morphology-based model. Current transients or sine-wave responses were simulated in NEURON (1-μs time step), applying square or sinusoidal voltage commands at the bouton. "Sample" frequencies were 200 and 50 kHz, respectively, for square and sinusoidal commands. Gaussian noise with realistic amplitude was generated by using the random number generator of MATHEMATICA. Noise was filtered at 100 kHz for the square-pulse responses and 10 kHz for the sine-wave responses (Gaussian filter), and points corresponding to the sample points of simulated traces were added. Square-pulse techniques (40) were tested as described above (for 0.02 ms $< t \leq$ 5 ms). Sine-wave techniques were tested as follows. Amplitude and phase of the resulting current were determined under steady-state conditions by fitting with a sinusoidal function or the sum of two sinusoidal functions. Amplitude and phase were converted into real and imaginary parts of the complex admittance. For the single sine-wave technique, real part, imaginary part, and dc were converted into C_m, R_a, and R_m by using equation 28 of Gillis (26). For the double sine-wave technique, real parts and imaginary parts for the two frequencies were converted into C_m, R_a, and R_m according to Rohlicek and Schmid (ref. 41; and see ref. 42). Changes were implemented as an increase in specific membrane capacitance or a decrease in specific resistance at a given position. To estimate the noise in C_m measurements due to thermal (Johnson) fluctuations in resistors, the power spectral density of the current noise was calculated as $S_I(f) = 4k_BT\ \mathrm{Re}[Y]$, where k_B is the Boltzmann constant, T is the absolute temperature, and Re[Y] is the real part of the admittance of the morphology-based model. The current variance at a given bandwidth was determined by using equations 48 and 49 of Gillis (26) and converted into the C_m noise by using a linear approximation [equation 50 of Gillis (26)].

Capacitance Measurements in Mossy Fiber Terminals. Capacitance measurements in whole-cell recorded hippocampal mossy fiber terminals were performed by using the "sine + dc" mode (25) of the software lock-in extension of PULSE in the EPC-9/2 amplifier. The sine-wave frequency was set to 5 kHz and the peak amplitude was set to ±50 mV; the holding potential was −100 mV. The internal two-pole Bessel filter for stimulus voltage was set to 20 μs, the three-pole Bessel filter for current was set to 10 kHz, and the sampling frequency was set to 50 kHz. The reversal potential of the dc was assumed to be 0 mV. To evoke release, 0.2- to 100-ms pulses to 0 mV were applied every 5–15 s. Measurements of capacitance changes were performed in a time interval <10 min after the whole-cell configuration was established. Because the membrane time constant τ_m of the bouton was ≈10 ms, a time interval of 3 τ_m (30 ms) after the pulse was considered invalid and blanked from the C_m recordings. ΔC_m was measured as the difference of C_m 50 ms before and 200–300 ms after the step, except in the experiments in which sine-wave and square-pulse techniques were compared (difference of C_m 2 s before and 2 s after the step). With these settings, the contribution of Na^+ channel gating charge movements is likely to be small (43, 44). First, the high sine-wave frequency will minimize gating charge effects (44). Second, the observed ΔC_m is unlikely to be generated directly by gating charge movements, which are much faster. It is also unlikely to arise from charge immobilization due to inactivation, because recovery of Na^+ channels from inactivation is complete within ≈20 ms in mossy fiber terminals (P.J., unpublished work). Finally, if significant charge immobilization occurred, we would expect a decrease of C_m, rather than an increase, after the pulse. To examine exocytosis, data were recorded at a resolution of one sine-wave cycle per data point. ΔC_m versus pulse duration relations were fitted with the sum of two exponentials. Only experiments with a signal-to-noise ratio (defined as ΔC_m at 10 ms divided by standard deviation of data points around the fitted curve) >2 were used. Amplitude-weighted decay time constants, τ_w, were calculated as $(A_1\tau_1 + A_2\tau_2)/(A_1 + A_2)$, where A_1 and A_2 are amplitudes and τ_1 and τ_2 are time constants of the components. In 1 of 26 recordings, the stimulus evoked a *negative* ΔC_m significantly larger than the recording noise; this experiment was excluded from the analysis. To examine endocytosis, data were averaged (25 sine-wave cycles per data point) and reduced (0.1 Hz) before storage. To determine the endocytosis time constant, traces were corrected for drifts by linear regression to the baseline, and the decay was fitted with a single exponential plus an offset. In a subset of experiments (Fig. 3*F*), 4 μM tetanus toxin, 0.3 mM DTT, and 0.1% BSA were added to the pipette solution. These experiments were performed at 34°C to promote the action of the toxin (45, 46).

Results

Standard capacitance measurement techniques were originally developed for single compartments (24–26), and it is unclear whether they can be extended to complex structures such as mossy fiber terminals (47–49). To determine the number of compartments necessary to represent the electrical structure of the mossy fiber terminals, we compared different models, starting from a model based on realistic morphological properties. A whole-cell-recorded biocytin-filled bouton was selected for reconstruction (Fig. 1*A*), and the previously recorded current transients were analyzed by direct fitting (Fig. 1*B*; ref. 37). This analysis gave a realistic electrical model of the bouton, with a membrane time constant, τ_m, of 9.4 ms. Next, several reduced models were tested. In the reconstructed bouton, a three-

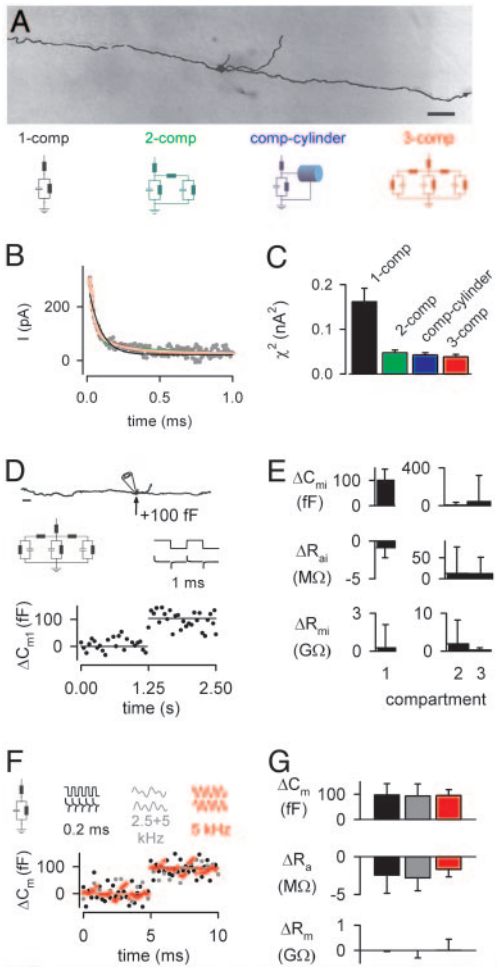

Fig. 1. Performance of capacitance measurement methods in a morphology-based electrical model of hippocampal mossy fiber terminals. (*A*) Photomicrograph of a bouton in *stratum lucidum* filled with biocytin during recording. The reconstructed morphology is shown superimposed (scale bar, 10 μm). (*B*) Average current transient (50 individual sweeps) in the same bouton in response to 5-ms pulses from −100 mV to −80 mV, superimposed with the predictions of the morphology-based model (white curve) and the simple compartmental models (see model schematics for color code) obtained by direct fitting (for 0.02 ms $< t \leq$ 5 ms). Direct fitting yielded an access resistance of 30.7 MΩ, a shunt resistance of 11.6 GΩ, an apparent specific membrane capacitance of 2.3 μF·cm^{-2}, a cytoplasmic resistivity of 124 Ω·cm, and a specific membrane resistance of 4,100 Ω·cm^2. Although the high apparent specific membrane capacitance suggests an underestimation of the surface area in the light-microscopic reconstruction, the model is expected to realistically capture the electrical properties. (*C*) Sum of squares of differences (χ^2) between recorded and calculated current transients for simple compartmental models ($n = 12$). When the same recorded transients were fitted with the sum of three exponentials, mean time constants of $\tau_1 = 21 \pm 1$ μs, $\tau_2 = 113 \pm 8$ μs, and $\tau_3 = 985 \pm 70$ μs were obtained. (*D*) Illustration of the three-compartment square-pulse technique [SQ_3; pulse duration 1 ms; current noise $\sigma =$ 50 pA/$\sqrt{50}$ (to simulate averaging of 50 traces)]. (*E*) Accuracy of ΔC_{mi}, ΔR_{ai}, and ΔR_{mi} ($i = 1 \ldots 3$) estimates for SQ_3. (*F*) Illustration of the one-compartment square-pulse technique (SQ_1; black; pulse duration 0.2 ms), the double sine-wave technique (SW_2; gray; frequencies 2.5 and 5 kHz), and the single sine-wave technique (SW_1; red; frequency 5 kHz). (*G*) Accuracy of ΔC_m, ΔR_a, and ΔR_m estimates for SQ_1, SW_2, and SW_1. In all cases, a capacitance increase of 100 fF was simulated at the bouton in the morphology-based model. The peak-to-peak amplitude of the command voltage was ±50 mV. Noise was $\sigma = 50$ pA and was filtered at 100 kHz for SQ_3 and SQ_1, and at 10 kHz for SW_2 and SW_1. In *E* and *G*, error bars represent standard deviations.

compartment model provided a markedly better fit than the one-compartment, two-compartment, or compartment-cylinder models; the three-compartment model was only slightly inferior to the morphology-based model (Fig. 1*B*). Among the reduced models, the three-compartment model gave the best fit of the current transients in 12 of 12 boutons (Fig. 1*C*). On average, the capacitance of the first compartment, presumably corresponding to the presynaptic terminal, was $C_{m1} = 1.44 \pm 0.20$ pF, whereas the capacitances of the higher compartments were 0.92 ± 0.14 and 3.33 ± 0.57 pF. For the three-compartment model, the mean access resistances, R_{ai} ($i = 1 \ldots 3$), were 20.8 ± 1.6, 128 ± 18, and 442 ± 55 MΩ, and the mean membrane resistances, R_{mi}, were 4.8 ± 0.7, 8.5 ± 1.6, and 2.7 ± 0.7 GΩ ($n = 12$). Thus C_{m1} is ≈10 times smaller than at the calyx of Held (32, 50).

The capacitance changes caused by exocytosis in mossy fiber terminals are expected to be near the absolute limits of resolution of established methods. Therefore, we systematically evaluated the performance of different techniques in the presence of recording noise, with a plausible presynaptic capacitance increase implemented at the bouton in the morphology-based model ($\Delta C_m = 100$ fF). We first considered using a three-compartment square-pulse technique (SQ_3) for real-time measurements of presynaptic capacitance changes. However, although the SQ_3 technique provided accurate estimates of the parameters of the first compartment, the temporal resolution was clearly insufficient, because averaging of several traces was necessary to obtain robust results (Fig. 1 *D* and *E*). We therefore explored alternative approaches, such as a one-compartment square-pulse technique (SQ_1; ref. 40), a double sine-wave technique (SW_2, "Rohlicek"; ref. 41), and a single sine-wave technique (SW_1, "sine + dc"; ref. 25). Identical command voltage amplitudes were chosen to allow a rigorous comparison. For a given temporal resolution, the accuracy of ΔC_m measurements (measured ΔC_m/implemented ΔC_m) was similar for the three techniques, but the best amplitude resolution was obtained with the single sine-wave approach (Fig. 1 *F* and *G*).

To be able to use the sine-wave method as a quantitative assay of exocytosis in mossy fiber terminals, we performed additional tests of accuracy and specificity (Fig. 2). The accuracy of the method in the morphology-based model was frequency dependent, rising with increasing sine-wave frequency (Fig. 2*A*). However, the predicted thermal noise of C_m measurements increased at higher frequencies, limiting the maximal sine-wave frequency that can be used experimentally to roughly 5 kHz (Fig. 2*B*). To examine the possibility of cross-talk of any parameters other than presynaptic capacitance onto the ΔC_m signal, we simulated plausible capacitance increases ($\Delta C_m = 100$ fF) and large conductance increases ($\Delta G_m = 0.5$ nS, corresponding to a maximal increase of ≈100%) at presynaptic and various axonal locations in the morphology-based model with 5 kHz sine-wave frequency (Fig. 2 *C* and *D*). Capacitance increases in the presynaptic compartment were monitored accurately, although they were associated with ΔR_a signals in the opposite direction. The relation between measured ΔC_m and implemented ΔC_{m1} was linear, and the accuracy of the measurement was 91% (Fig. 2*C Left*). Changes in the access resistance ΔR_{a1} were monitored precisely, without effect on the other parameters (Fig. 2*C Center*). Conductance increases were also determined accurately, although they were associated with a small positive ΔC_m signal (Fig. 2*C Right*). For capacitance increases in more distant compartments, the ΔC_m signal decayed steeply as a function of distance from the presynaptic site (Fig. 2*D Left*; ≈3 μm per e-fold change), whereas for conductance increases in more distant compartments the ΔR_m signal declined gradually (Fig. 2*D Right*; 56 μm per e-fold change). Interestingly, the sign of ΔR_a after simulated exocytosis reversed at a distance of ≈2 μm (Fig. 2*D Left*). In conclusion, the high-frequency sine-wave technique showed a high spatial resolution and specificity, consistent with earlier conclusions (21). Cross-talk to the C_m trace was minimal, except for large conductance changes in the presynaptic terminal; however, such conductance changes would be readily de-

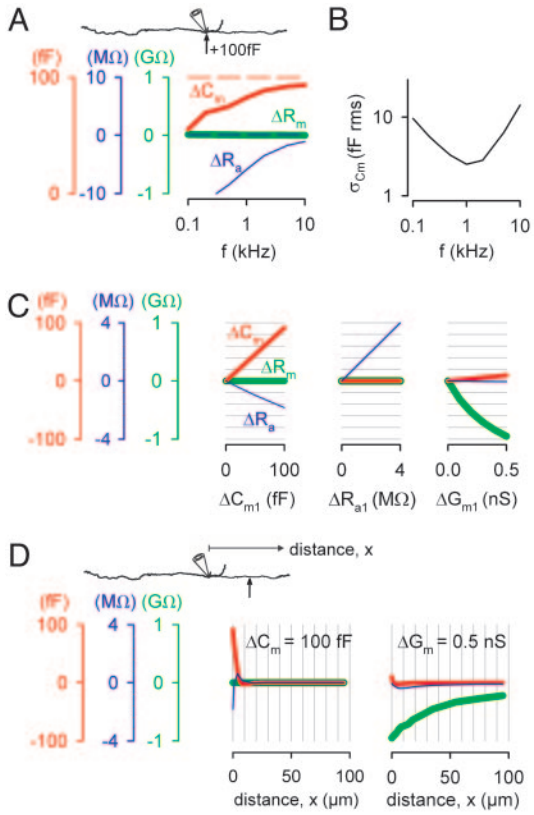

Fig. 2. High-frequency sine-wave techniques provide an accurate and specific assay of exocytosis from mossy fiber terminals. (*A*) Accuracy of ΔC_m (red), ΔR_a (blue), and ΔR_m (green) estimates, plotted against sine-wave frequency *f*, for a ΔC_m of 100 fF at the bouton in the morphology-based model. Model parameters were identical to those specified in the legend of Fig. 1*B*. (*B*) Predicted thermal noise of C_m estimates at a bandwidth of 5 kHz, plotted against sine-wave frequency. Noise was calculated from the complex admittance of the morphology-based model. (*C*) ΔC_m, ΔR_a, and ΔR_m, measured by a 5-kHz sine-wave technique after changes in membrane capacitance ΔC_{m1} (*Left*), access resistance ΔR_{a1} (*Center*), or membrane conductance ΔG_{m1} (*Right*) in the first compartment (bouton) of the morphology-based model. (*D*) ΔC_m, ΔR_a, and ΔR_m, measured by the sine-wave technique after changes in membrane capacitance ($\Delta C_m = 100$ fF; *Left*) and membrane conductance ($\Delta G_m = 0.5$ nS; *Right*) in different axonal compartments, plotted against the location of the change (*x*, measured from the point of emergence of the axon from the bouton). Similar calculations were performed to address three additional potential errors: (*i*) Errors in reversal potential setting ($E_{rev} = -50$ mV instead of 0 mV); results were almost identical. (*ii*) Phase errors (1°); results were very similar, except for a larger ΔR_a in *C Center*. (*iii*) Incomplete pipette compensation (first four cylinders of pipette model taken from ref. 59, 150 fF total pipette capacitance); results were similar except in *C Left* (smaller ΔR_a) and *C Center* (larger $-\Delta C_m$).

tected in the R_m trace. As the sign of ΔR_a reverses with distance, the ΔR_a signal provides information about the locus of the capacitance increase, with negative values indicating changes directly in the presynaptic terminal.

To probe fundamental properties of exocytosis, we applied the high-frequency sine-wave technique to whole-cell recorded mossy fiber terminals (Fig. 3). To induce transmitter release, Ca^{2+} inflow was evoked by 30-ms voltage pulses in the presence of blockers of voltage-gated Na^+ and K^+ channels; a stimulus amplitude of 0 mV was chosen to maximize the presynaptic Ca^{2+} current (23). In the presynaptic recording illustrated, the 30-ms stimulus evoked an increase of C_m by 23 fF, a decrease of R_a by 0.12 MΩ, and a decrease of R_m by 0.037 GΩ (Fig. 3*A*). On average, a 30-ms pulse led to a mean ΔC_m of 101 ± 48 fF (Fig. 3*B*; $n = 12$). The size of ΔC_m was only weakly correlated with the peak amplitude of the presynaptic Ca^{2+} current (Fig. 3 *C* and *D*; $r = 0.24$, $P > 0.05$), indicating that the amplitude of ΔC_m was not limited by presynaptic Ca^{2+} inflow.

The results raise additional questions: Are the observed capacitance increases generated at the presynaptic terminal, and if so, are they unequivocally related to exocytosis? A highly significant correlation between ΔC_m and $-\Delta R_a$ was found ($r = 0.91$, $P < 0.001$), as quantitatively predicted from the bouton models (Fig. 3*E*, curves). This is consistent with the hypothesis that the capacitance increases were generated in the mossy fiber terminal rather than the axon or the filopodial extensions (47–49). Furthermore, 4 μM tetanus neurotoxin applied to the intracellular solution blocked the capacitance signals; ΔC_m in the presence of tetanus toxin was 18% of ΔC_m in interleaved controls under identical recording conditions (Fig. 3*F*; $P < 0.05$). Because tetanus toxin selectively cleaves synaptobrevin (45, 46), these experiments show that the capacitance signals were caused by exocytosis. In conclusion, our results indicate that voltage pulses evoke large exocytosis-related capacitance increases in hippocampal mossy fiber terminals, comparable in size to those recently reported in the calyx of Held (14, 19). With a single-vesicle ΔC_m of ≈70 aF, obtained from a mean clear vesicle diameter of 47 nm in mossy fiber terminals (figure 7D of ref. 52; see refs. 19 and 53) and a specific membrane capacitance of 1 μF cm^{-2}, the ΔC_m evoked by 30-ms pulses corresponds to the fusion of ≈1,400 vesicles. A potential caveat is that mossy fiber terminals contain a small proportion of large dense-core vesicles, which will lead to an overestimation of pool size.

Capacitance measurements allowed us to quantify rates in the synaptic vesicle cycle at hippocampal mossy fiber synapses (Fig. 3 *G–I*). To determine the size of the releasable pool and the maximal rate of exocytosis, the length of the depolarizing pulse was varied between 0.2 and 100 ms, and ΔC_m was plotted against pulse duration (Fig. 3*G*). ΔC_m rose steeply for short pulses but approached saturation with longer pulses. In the experiment shown, the time course was biexponential, with time constants of 1.6 and 22 ms, suggesting that readily releasable and slowly releasable pools coexist at mossy fiber synapses (51). In the experiment illustrated, the amplitude-weighted time constant (τ_w) was 15 ms; on average, τ_w was 21 ± 3 ms ($n = 3$). The maximal release rate, determined as pool size (for 30-ms pulse) divided by τ_w, was ≈70 vesicles per millisecond. Thirty-millisecond pulses evoked near-maximal ΔC_m signals (Fig. 3*G*), indicating that the ΔC_m obtained with this pulse duration is an adequate measure of the size of the releasable pool of synaptic vesicles. After a stimulus that produced pool depletion, the capacitance signal decayed back to baseline within several seconds, presumably reflecting membrane retrieval by endocytosis (Fig. 3 *H* and *I*). On average, the endocytosis time constant was 9.0 ± 5.5 s ($n = 3$) and the extent of endocytosis measured 10 s after the peak was 105 ± 53% ($n = 4$). With our estimate of a releasable pool size of ≈1,400 vesicles, the time constant corresponds to a maximal rate of endocytosis of ≈160 vesicles per s.

Discussion

In the present paper, three major findings are reported. First, we define the conditions under which techniques for capacitance measurements can be applied to small presynaptic terminals comprised of multiple electrical compartments. Second, we report a direct presynaptic measurement of the size of the releasable vesicle pool at a cortical glutamatergic synapse. We estimate that the releasable vesicle pool in mossy fiber terminals is comprised of ≈1,400 vesicles. Thus, the pool is substantially larger than previously reported for glutamatergic synapses in primary culture (27, 28). This apparent disagreement is probably due to differences between both synapse types and assays (pre- versus postsynaptic). Third, we made real-time measurements of endocytosis in mossy fiber terminals. Whereas exocytosis occurs

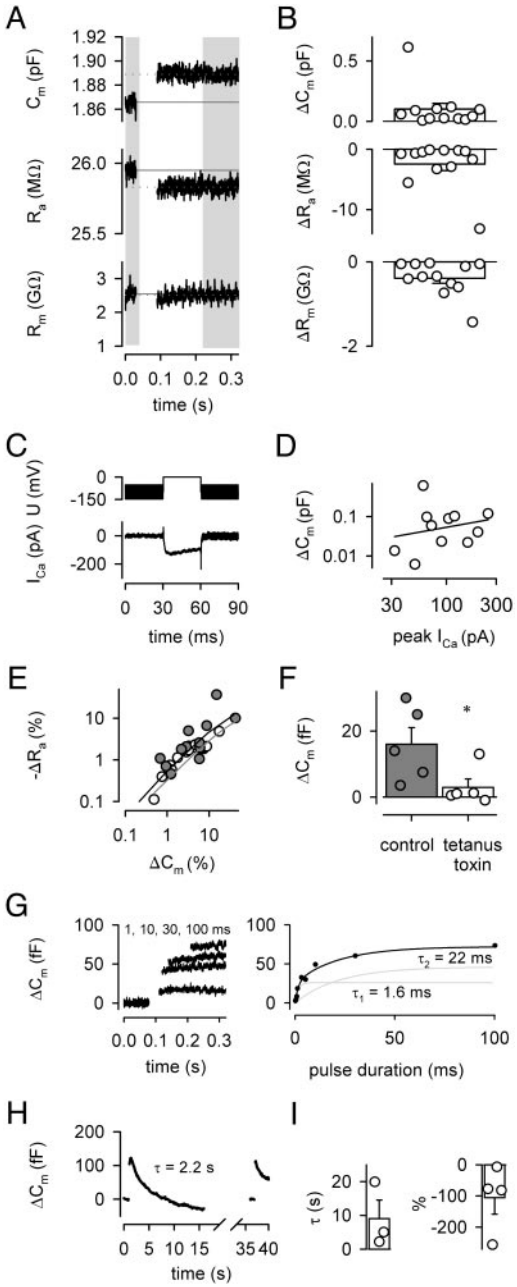

Fig. 3. Large pool size and rapid vesicle cycling in hippocampal mossy fiber terminals. (*A*) Changes in C_m, R_a, and R_m evoked by a 30-ms pulse. Vertical gray bars indicate regions for analysis. (*B*) Summary plots of ΔC_m, ΔR_a, and ΔR_m evoked by 30-ms pulses. Bars represent means ± SEM; symbols indicate individual experiments ($n = 12$). In three experiments, sine-wave method SW_1 and square-pulse technique SQ_3 (100-mV amplitude) were applied in an interleaved manner at 2 Hz. In these experiments, SW_1 gave $\Delta C_m = 22$ fF, $\Delta R_a = -0.6$ MΩ, and $\Delta R_m = -0.6$ GΩ, in approximate agreement with the results of SQ_3 ($\Delta C_{m1} = 41$ fF, $\Delta R_{a1} = -0.3$ MΩ, and $\Delta R_{m1} = -0.08$ GΩ); corresponding C_m and C_{m1} noise values were 2.3 fF versus 18.4 fF. (*C*) Voltage-command and corresponding Ca^{2+} current (corrected for leak and capacitive current) in the same bouton shown in *A*. Note the sine-wave stimulation before and after the stimulus (5 kHz, ±50 mV). (*D*) Double-logarithmic scatter plot of ΔC_m versus peak Ca^{2+} current. The line represents linear regression. (*E*) Double-logarithmic scatter plot of $-\Delta R_a$ versus ΔC_m. Filled circles represent data obtained with the 30-ms pulses shown in *B*; open circles illustrate experiments with different pulse durations (0.2–100 ms; $n = 33$ total; seven data points outside plotting range). Lines represent predictions of the morphology-based (black) and three-compartment models (gray). (*F*) ΔC_m signals evoked by 5-ms pulses in control conditions and in the presence of 4 μM tetanus toxin (recording temperature 34°C; *, $P < 0.05$). The peak Ca^{2+} current was not different in the two sets of measurements ($P > 0.5$). (*G Left*) ΔC_m signals evoked by 1-, 10-, 30-, and 100-ms test pulses, preceded by a 1.2-ms prepulse to 65 mV to maximally activate Ca^{2+} channels without Ca^{2+} inflow. A rapid component of endocytosis was not apparent under these conditions (19). (*G Right*) ΔC_m plotted against test-pulse duration. Note that ΔC_m saturates at a pulse duration of ≈30 ms. The continuous curve represents a biexponential function fitted to the data points ($\tau_1 = 1.6$ ms, $\tau_2 = 22$ ms); exponential components are shown superimposed. Data points represent single measurements, except for pulse durations <1 ms (means of five measurements). (*H*) ΔC_m signals evoked by two 30-ms pulses shown on a slow time scale. The membrane capacitance decays back to baseline with a time constant of 2.2 s. (*I*) Summary plot of endocytosis time constants (*Left*; $n = 3$) and percentage of recovery after 10 s (*Right*; $n = 4$). Note the variable endocytosis time course and extent, as well as the excess endocytosis in one recording.

within milliseconds, endocytosis proceeds on a time scale of seconds.

Whereas sine-wave techniques for capacitance measurements were originally developed for single-compartment structures (25, 26), mossy fiber terminals are electrically complex. Presumably, the three compartments in our reduced representation (Fig. 1*B*) represent the presynaptic terminal, the axon, and the filopodial extensions (47–49). Extensive tests based on the morphology-based model show that high-frequency sine-wave techniques probe ΔC_m accurately. However, the structural complexity introduces a correlation between ΔC_m and $-\Delta R_a$. Intuitively, this apparent ΔR_a can be understood as follows. If a complex structure with distributed capacitances and resistors is approximated with a single-compartment formalism, the measured R_a is expected to be the weighted mean of R_{a1}, $R_{a1} + R_{a2}$, . . . , $R_{a1} + \cdots + R_{an}$, with weights related to the capacitances C_{mi} of the ith compartment ($i = 1 \ldots n$). If an increase in C_m occurs in the first compartment, the weight of R_{a1} increases and the measured R_a shifts toward R_{a1}. In contrast, if an increase of C_m occurs in higher compartments, R_a shifts in the opposite direction. Thus, the sign of ΔR_a provides information about the location of the change. For the mossy fiber terminals, the negative ΔR_a implies that the ΔC_m signal is generated at the presynaptic terminal rather than filopodial extensions or axon.

Using presynaptic capacitance measurements, we derived a quantitative picture of exo- and endocytosis at mossy fiber terminals. The releasable pool is comprised of ≈1,400 vesicles. With 37 active zones per large mossy fiber terminal based on serial electron microscopy (47), this translates into ≈40 vesicles per active zone. Because these ≈40 vesicles are released within a 30-ms time interval (Fig. 3*G*), the present results argue strongly in favor of multivesicular release (31, 32) but against lateral inhibition (54) or fast adaptation of the Ca^{2+} sensor (55) at this synapse under our conditions. For 37 active zones (47), the maximal rate of endocytosis after complete pool depletion can be estimated as (≈160 vesicles per s)/37 = ≈4 vesicles per s per active zone. These quantitative results in mossy fiber terminals contrast with previous data at the calyx of Held. Although the size of the releasable pool is comparable at the two types of synapses (≈1,400 and ≈700 to ≈8,000 vesicles, respectively; refs. 14, 19, 29, 30, and 32), the number of releasable vesicles per active zone is substantially larger (≈40 versus ≈4,000/554 = ≈7; ref. 53) and the rate of endocytosis per active zone after pool depletion is faster at the mossy fiber terminals than at the calyx (≈4 versus ≈0.5 vesicles per s; refs. 14 and 19).

Previous studies showed that the brief presynaptic action potential in mossy fiber terminals (22) is a highly efficient stimulus for activating presynaptic Ca^{2+} channels (23). The present results, however, suggest that the Ca^{2+} inflow associated with a single presynaptic action potential (half-duration 580 μs; ref. 23) releases only a very small fraction of the vesicle pool (Fig. 3*G*). In contrast, high-frequency trains of presynaptic action potentials, perhaps in

combination with action potential broadening (22), will be needed to release a larger fraction. At the mossy fiber–cornu ammonis area 3 (CA3) pyramidal neuron synapse, high-frequency stimulation leads to an almost 10-fold increase in synaptic strength, because of frequency facilitation, posttetanic potentiation, and long-term potentiation (56, 57). Because all of these activity-dependent changes are probably expressed presynaptically, the large number of vesicles per active zone at the mossy fiber synapse provides a straightforward explanation for their unique extent. The large pool may also help to understand the impact of mossy fiber synaptic transmission during presynaptic spike trains *in vivo* (58).

We thank Drs. E. Neher and R. Schneggenburger for advice during the implementation of capacitance measurements, H. Bigalke for providing tetanus toxin, and J. Bischofberger, E. Neher, and G. Stuart for critically reading an earlier version of the manuscript. This work was supported by the Deutsche Forschungsgemeinschaft (SFB 505/C12) and the Alexander-von-Humboldt Foundation.

1. Katz, B. (1969) *The Release of Neural Transmitter Substances* (Liverpool Univ. Press, Liverpool, U.K.).
2. Betz, W. J. & Bewick, G. S. (1992) *Science* **255,** 200–203.
3. Beaumont, V. & Zucker, R. S. (2000) *Nat. Neurosci.* **3,** 133–141.
4. Llinás, R. (1999) *The Squid Giant Synapse* (Oxford Univ. Press, New York).
5. Adler, E. M., Augustine, G. J., Duffy, S. N. & Charlton, M. P. (1991) *J. Neurosci.* **11,** 1496–1507.
6. Forsythe, I. D. (1994) *J. Physiol. (London)* **479,** 381–387.
7. Borst, J. G. G., Helmchen, F. & Sakmann, B. (1995) *J. Physiol. (London)* **489,** 825–840.
8. Wang, L.-Y. & Kaczmarek, L. K. (1998) *Nature* **394,** 384–388.
9. von Gersdorff, H. & Matthews, G. (1994) *Nature* **367,** 735–739.
10. von Gersdorff, H., Sakaba, T., Berglund, K. & Tachibana, M. (1998) *Neuron* **21,** 1177–1188.
11. Bliss, T. V. P. & Collingridge, G. L. (1993) *Nature* **361,** 31–39.
12. Zalutsky, R. A. & Nicoll, R. A. (1990) *Science* **248,** 1619–1624.
13. Yeckel, M. F., Kapur, A. & Johnston, D. (1999) *Nat. Neurosci.* **2,** 625–633.
14. Sun, J.-Y. & Wu, L.-G. (2001) *Neuron* **30,** 171–182.
15. Neher, E. & Sakaba, T. (2001) *J. Neurosci.* **21,** 444–461.
16. Ryan, T. A. (2003) *Proc. Natl. Acad. Sci. USA* **100,** 2171–2173.
17. Pyle, J. L., Kavalali, E. T., Piedras-Rentería, E. S. & Tsien, R. W. (2000) *Neuron* **28,** 221–231.
18. Gillespie, J. I. (1979) *Proc. R. Soc. London Ser. B* **206,** 293–306.
19. Sun, J.-Y., Wu, X.-S. & Wu, L.-G. (2002) *Nature* **417,** 555–559.
20. Hsu, S.-F. & Jackson, M. B. (1996) *J. Physiol. (London)* **494,** 539–553.
21. Mennerick, S., Zenisek, D. & Matthews, G. (1997) *J. Neurophysiol.* **78,** 51–62.
22. Geiger, J. R. P. & Jonas, P. (2000) *Neuron* **28,** 927–939.
23. Bischofberger, J., Geiger, J. R. P. & Jonas, P. (2002) *J. Neurosci.* **22,** 10593–10602.
24. Neher, E. & Marty, A. (1982) *Proc. Natl. Acad. Sci. USA* **79,** 6712–6716.
25. Lindau, M. & Neher, E. (1988) *Pflügers Arch.* **411,** 137–146.
26. Gillis, K. D. (1995) in *Single-Channel Recording*, eds. Sakmann, B. & Neher, E. (Plenum, New York), pp. 155–198.
27. Stevens, C. F. & Tsujimoto, T. (1995) *Proc. Natl. Acad. Sci. USA* **92,** 846–849.
28. Rosenmund, C. & Stevens, C. F. (1996) *Neuron* **16,** 1197–1207.
29. Schneggenburger, R., Meyer, A. C. & Neher, E. (1999) *Neuron* **23,** 399–409.
30. Bollmann, J. H., Sakmann, B. & Borst, J. G. G. (2000) *Science* **289,** 953–957.
31. Wadiche, J. I. & Jahr, C. E. (2001) *Neuron* **32,** 301–313.
32. Taschenberger, H., Leão, R. M., Rowland, K. C., Spirou, G. A. & von Gersdorff, H. (2002) *Neuron* **36,** 1127–1143.
33. Ryan, T. A., Reuter, H., Wendland, B., Schweizer, F. E., Tsien, R. W. & Smith, S. J. (1993) *Neuron* **11,** 713–724.
34. Geiger, J. R. P., Bischofberger, J., Vida, I., Fröbe, U., Pfitzinger, S., Weber, H. J., Haverkampf, K. & Jonas, P. (2002) *Pflügers Arch.* **443,** 491–501.
35. Tsien, R. & Pozzan, T. (1989) *Methods Enzymol.* **172,** 230–262.
36. Bartos, M., Vida, I., Frotscher, M., Meyer, A., Monyer, H., Geiger, J. R. P. & Jonas, P. (2002) *Proc. Natl. Acad. Sci. USA* **99,** 13222–13227.
37. Clements, J. D. & Redman, S. J. (1989) *J. Physiol. (London)* **409,** 63–87.
38. Hines, M. L. & Carnevale, N. T. (1997) *Neural Comput.* **9,** 1179–1209.
39. Major, G., Evans, J. D. & Jack, J. J. B. (1993) *Biophys. J.* **65,** 450–468.
40. Thompson, R. E., Lindau, M. & Webb, W. W. (2001) *Biophys. J.* **81,** 937–948.
41. Rohlicek, V. & Schmid, A. (1994) *Pflügers Arch.* **428,** 30–38.
42. Barnett, D. W. & Misler, S. (1997) *Biophys. J.* **72,** 1641–1658.
43. Horrigan, F. T. & Bookman, R. J. (1994) *Neuron* **13,** 1119–1129.
44. Kilic, G. & Lindau, M. (2001) *Biophys. J.* **80,** 1220–1229.
45. Xu, T., Binz, T., Niemann, H. & Neher, E. (1998) *Nat. Neurosci.* **1,** 192–200.
46. Südhof, T. C. (1995) *Nature* **375,** 645–653.
47. Chicurel, M. E. & Harris, K. M. (1992) *J. Comp. Neurol.* **325,** 169–182.
48. Acsády, L., Kamondi, A., Sík, A., Freund, T. & Buzsáki, G. (1998) *J. Neurosci.* **18,** 3386–3403.
49. Maccaferri, G., Tóth, K. & McBain, C. J. (1998) *Science* **279,** 1368–1370.
50. Borst, J. G. G. & Sakmann, B. (1998) *J. Physiol. (London)* **506,** 143–157.
51. Sakaba, T. & Neher, E. (2001) *Neuron* **32,** 1119–1131.
52. Henze, D. A., McMahon, D. B. T., Harris, K. M. & Barrionuevo, G. (2002) *J. Neurophysiol.* **87,** 15–29.
53. Sätzler, K., Söhl, L. F., Bollmann, J. H., Borst, J. G. G., Frotscher, M., Sakmann, B. & Lübke, J. H. R. (2002) *J. Neurosci.* **22,** 10567–10579.
54. Abenavoli, A., Forti, L., Bossi, M., Bergamaschi, A., Villa, A. & Malgaroli, A. (2002) *J. Neurosci.* **22,** 6336–6346.
55. Hsu, S.-F., Augustine, G. J. & Jackson, M. B. (1996) *Neuron* **17,** 501–512.
56. Salin, P. A., Scanziani, M., Malenka, R. C. & Nicoll, R. A. (1996) *Proc. Natl. Acad. Sci. USA* **93,** 13304–13309.
57. Alle, H., Jonas, P. & Geiger, J. R. P. (2001) *Proc. Natl. Acad. Sci. USA* **98,** 14708–14713.
58. Henze, D. A., Wittner, L. & Buzsáki, G. (2002) *Nat. Neurosci.* **5,** 790–795.
59. Roth, A. & Häusser, M. (2001) *J. Physiol. (London)* **535,** 445–472.